Available online at www.sciencedirect.com
SCIENCE DIRECT®
International Journal of Heat and Fluid Flow 24 (2003) 795–806
International Journal of HEAT AND FLUID FLOW
www.elsevier.com/locate/ijhff

The turbulent character and pressure loss produced by periodic symmetric ribs in a circular duct

Stephen A. Jordan

Naval Undersea Warfare Center, Code 74 Bldg. 1346/4, Newport, RI 02841, USA

Received 8 December 2002; accepted 16 July 2003

Abstract

The structural character and steady-state statistics of the turbulence inside a rib-wall circular duct is investigated by the large-eddy simulation (LES) methodology. The impetus of this study is to gain an understanding of the principle physics attributing to minimizing the pressure recovered (or maximizing the pressure loss) within the core flow. For a rib periodicity with height (h) to pitch (p) ratio $p/h = 5$, the computational results show that the majority of turbulence produced due to the rib's presence is concentrated near the rib crest leading edge. Pairs of counter-rotating streamwise vortices form soon after the leading edge that are quickly convected radially toward the core flow. The turbulent activity within the duct trough region is negligible compared to the turbulence levels of the core flow. At this rib periodicity, the separated shear layers from the trailing edge of each rib nearly reattach to the trough floor before reaching the next rib. The resultant irrecoverable pressure loss in the form a centerline frictional coefficient is verified by an 'at-sea' test on board a US Navy submarine. Based on the duct diameter, their Reynolds numbers are $Re_D^{LES} = 8 \times 10^3$ and $(Re_D^{exp})_{avg} = 4 \times 10^6$, respectively.

Keywords: Rib-wall ducts; Large-eddy simulation; Turbulent shear layers; Pressure loss

1. Introduction

Roughening surfaces with small discrete ribs is thoroughly understood qualitatively for enhancing and controlling mass and heat transfer rates. This knowledge arose largely from the experimental and numerical investigations that demonstrated their importance in designing efficient ducts for mechanical systems such as aircraft engines and nuclear reactors. The ribs themselves are typically mounted periodically along the inner walls of the duct and generate new turbulent regions within the core streamwise flow. This enhanced turbulent activity greatly improves the mixing and/or cooling characteristics of the ribbed surface over the smooth-walled duct. Generally, the accompanying pressure loss is viewed as a design penalty of the rib element, but in certain applications this consequence is an effective means for controlling the pressure gradient within the duct. For example, Navy design engineers require strict control over the extent of the pressure recovered inside submarine hull recessed cavities and vehicle launchways to insure successful undersea operations during reconnaissance and defense missions.

The flow characteristics of ribbed-wall ducts in the fully rough regime (independent of Reynolds number) fall basically under one of two categories. Perry et al. (1969) termed roughened surfaces with $p/h > 4$ as 'k-type' meaning that the rib presence disturbs the core flow structure; p/h denotes the rib pitch (p) scaled by its height (h). This defined cut-off is beyond that of roughened flat plates where the outer flow is affected by the ribs presence for $p/h > 1$ (Okamoto et al., 1993; Keirsbulck et al., 2002). In both cases, large-scale turbulent vortices shed from the rib crests whose downstream structure remains intact while convected by the adjacent streamwise flow. Typically, the integral scale of these structures correlates well with the respective rib height. By contrast, roughened surfaces within ducts with $p/h \leqslant 4$ signify the generation of confined vortical structures oscillating between the ribs with minimal influence on the core flow characteristics. Outside of a very small length near the leading edge, the flow remains largely attached along the rib crests. Unlike a 'k-type' rough wall, the mean streamwise

E-mail address: jordansa@npt.nuwc.navy.mil (S.A. Jordan).

0142-727X/$ - see front matter © 2003 Elsevier Inc. All rights reserved.
doi:10.1016/j.ijheatfluidflow.2003.07.001

outer flow of the 'd-type' roughness can be quantified by the logarithmic law (using inner variables) that extends down to the viscous sublayer along the rib crests. Concurrently, the inner flow of the 'd-type' wall is essentially defined by the boundaries of the trough regions that lie between the closely spaced ribs.

The present paper deals with the 'k-type' roughness as an effective mechanism for controlling the mean pressure loss (or in this case optimizing the mean pressure recovery) within a cylindrical duct. We are specifically interested in investigating the structural content and the new turbulent production characteristics surrounding the ribs that attribute to the rise in the mean static pressure loss of the outer flow. Notably, we can favor the study by selecting the optimum p/h ratio that generates a high streamwise pressure loss through turbulence ingestion. However, in the literature one will find little agreement among the empirical parameters for approximating the fictional factor (f) of a 'k-type' rib-roughened wall in the fully turbulent regime (see Fig. 1 and Table 1). In terms of the static pressure loss gradient ($\mathrm{d}p/\mathrm{d}z$), duct diameter (D), density (ρ), and bulk velocity (u_b), the local friction factor can be calculated using the modified logarithmic law (Whitehead, 1976; Webb et al., 1971; Wassel and Mills, 1979; Han, 1988):

$$f = -\frac{2D}{\rho u_\mathrm{b}^2}\cdot\frac{\mathrm{d}p}{\mathrm{d}z} = 2\left[\frac{1}{\kappa}\ln\left(\frac{D}{2h}\right) + u_h^+ - B\right]^{-2} \tag{1}$$

where the roughness function, $u_h^+ = C(p/h)^\beta$, accounts for the increased pressure loss due to the roughened surface. Given a specific (or equivalent) roughness height, the choice of the roughness pitch for approximating the pressure loss is not easily obtained in view of these relationships. The disparity among them arises due to several factors that are centered on each respective experiment, such as the test section boundaries, h/D (or h/D_h) ratio and range of p/h ratios studied.

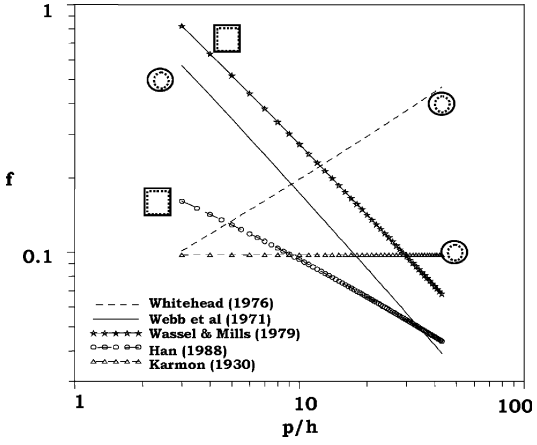

Fig. 1. Friction factors (f) as a function of the rib pitch (p) to height (h) ratio for circular and square roughened ducts.

Table 1
Referenced values used for the parameters in Eq. (1) for estimating the friction factor as plotted in Fig. 1

Reference	κ	B	C	β
Whitehead (1976)	0.41	4.50	6.53	−0.24
Webb et al. (1971)	0.41	3.75	0.95	0.53
Wassel et al. (1979)	0.41	3.75	$1 - h/R_h$	0.50
Han (1988)	0.40	3.50	1.43	0.35
Karman (1930)	0.40	1.20	–	–

Due to the lack of a unique choice of p/h for enhancing the turbulent character surrounding the ribs, we will acknowledge the observations made by Berger and Hau (1979). They reported the local mean mass and heat transfer distributions of a fully-developed turbulent flow within a circular duct whose inside surface was roughened by periodic square shaped ribs. After conducting numerous tests with parametric ranges $3 \leqslant p/h \leqslant 10$ and $1 \times 10^4 \leqslant Re_\mathrm{D} \leqslant 2.5 \times 10^5$ (based on pipe diameter, D), Berger and Hau observed highest mass transfer (and consequently maximum pressure loss) when $p/h = 5$ in the fully turbulent regime. Although no flow visualization results were shown, they suggested that peak mixing occurred when reattachment of the free shear layer in the trough region coincided with separation due to the presence of the next rib. Okamoto et al. (1993) agreed with their reasoning, but they detected maximum turbulent intensities, heat transfer and pressure loss when $p/h = 9$ for ribs mounted on a flat plate. At $p/h = 5$, their measurements gave low turbulent mixing, non-reattachment and self-preserving free shear-layer profiles downstream of each subsequent rib.

In the present paper, the turbulent characteristics of the cylindrical ribbed duct with $p/h = 5$ reflect computations at $Re_\mathrm{D} = 8000$ ($Re_\theta = 760$) using the large-eddy simulation (LES) methodology. Since the energy-dominate scales of the turbulent field are the primary mechanism attributing to the pressure loss, this numerical technique is well suited for this purpose. By definition, the impetus of LES is full resolution of the energy-bearing scales of the turbulent motion while modeling the smaller scales that tend towards homogeneous and isotropic conditions. The spatial extent in the computations is sufficient to fully resolve the important turbulent structures and statistical quantities that originate from the rib's presence. Comparisons of the computed mean quantities are made to '*at-sea*' measurements that were taken within a full-scale prototype device, which was installed onboard a US Navy submarine. Although the latter quantities reflect measurements at $3.2 \times 10^6 \leqslant Re_\mathrm{D} \leqslant 4.6 \times 10^6$ ($1.9 \times 10^4 \leqslant Re_\theta \leqslant 2.8 \times 10^4$), we will demonstrate that the salient turbulent statistics are adequately self-similar to yield equivalent mean parameters in both ducts.

2. Governing equations and solution method

Proper spatial resolution of the dominant viscous activity in the cylindrical duct demands stretch grids

around the rib elements. Development of a LES formulation applicable to this boundary fitted grid topology requires transformation and filtering of the cylindrical coordinate form of the incompressible Navier–Stokes and continuity equations to a curvilinear coordinate equation system. We can develop these equations according to the procedure suggested by Jordan (1999) where the first spatial operation is formal transformation of each term. The resultant system is a set of direct numerical simulation (DNS) equations that are applicable to a cylindrical computational domain,

$$\frac{\partial \sqrt{g}\xi^k_{x_j} q_j}{\partial \xi^k} = 0 \tag{2}$$

$$\frac{\partial r\sqrt{g}v_x}{\partial t} + \frac{\partial \sqrt{g}\xi^k_{x_j} q_j v_x}{\partial \xi^k} = -\frac{\partial r\sqrt{g}\xi^k_x p}{\partial \xi^k} + \frac{1}{Re}\frac{\partial}{\partial \xi^k}\left[\sqrt{g}g^{k\lambda}\frac{\partial v_x}{\partial \xi^\lambda}\right] \tag{3a}$$

$$\begin{aligned}\frac{\partial r\sqrt{g}v_r}{\partial t} + \frac{\partial \sqrt{g}\xi^k_{x_j} q_j v_r}{\partial \xi^k} - \sqrt{g}v_\theta v_\theta \\ = -r\frac{\partial \sqrt{g}\xi^k_r p}{\partial \xi^k} + \frac{1}{Re}\left[\frac{\partial}{\partial \xi^k}\left(\sqrt{g}g^{k\lambda}\frac{\partial v_r}{\partial \xi^\lambda}\right)\right. \\ \left. -\frac{1}{r}\left(\sqrt{g}v_r + 2\frac{\partial \sqrt{g}\xi^k_\theta v_\theta}{\partial \xi^k}\right)\right]\end{aligned} \tag{3b}$$

$$\begin{aligned}\frac{\partial r\sqrt{g}v_\theta}{\partial t} + \frac{\partial \sqrt{g}\xi^k_{x_j} q_j v_\theta}{\partial \xi^k} + \sqrt{g}v_r v_\theta \\ = -\frac{\partial \sqrt{g}\xi^k_\theta p}{\partial \xi^k} + \frac{1}{Re}\left[\frac{\partial}{\partial \xi^k}\left(\sqrt{g}g^{k\lambda}\frac{\partial v_\theta}{\partial \xi^\lambda}\right)\right. \\ \left. -\frac{1}{r}\left(\sqrt{g}v_\theta - 2\frac{\partial \sqrt{g}\xi^k_\theta v_r}{\partial \xi^k}\right)\right]\end{aligned} \tag{3c}$$

where each term is shown in its non-dimensional conservative form: $x_j = \langle x, r, \theta\rangle$, $q_j = \langle rv_x, rv_r, v_\theta\rangle$ and $g^{k\lambda} = h_j \xi^k_{x_j}\xi^\lambda_{x_j}$, where $h_j = \langle r, r, 1/r\rangle$. The coefficients $\xi^k_{x_j}$ and $\sqrt{g}$ denote the metrics and the Jacobian of the transformation, respectively. To obtain the corresponding LES formulation, the cylindrical system in (2) and (3) must now be spatially filtered. Assuming that the filter width and local grid spacing are equal, the resolved and filtered turbulent fields are mathematically the same. The differentiation and filtering commute similar to the filter operation applied to the Navier–Stokes equations in Cartesian coordinates. The resultant grid-filtered equations in curvilinear coordinates for cylindrical geometries become

$$\frac{\partial \overline{U}}{\partial \xi} + \frac{\partial \overline{V}}{\partial \eta} + \frac{\partial \overline{W}}{\partial \zeta} = 0 \tag{4}$$

$$\frac{\partial r\sqrt{\tilde{g}}\bar{v}_x}{\partial t} + \frac{\partial \overline{U}^k \bar{v}_x}{\partial \xi^k} = -\frac{\partial r\sqrt{\tilde{g}}\tilde{\xi}^k_x \bar{p}}{\partial \xi^k} + \frac{\partial \sigma^k_x}{\partial \xi^k} + \frac{1}{Re}\frac{\partial}{\partial \xi^k}\left(\sqrt{\tilde{g}}\tilde{g}^{k\lambda}\frac{\partial \bar{v}_x}{\partial \xi^\lambda}\right) \tag{5a}$$

$$\begin{aligned}\frac{\partial r\sqrt{\tilde{g}}\bar{v}_r}{\partial t} + \frac{\partial \overline{U}^k \bar{v}_r}{\partial \xi^k} - \sqrt{\tilde{g}}\bar{v}_\theta \bar{v}_\theta \\ = -r\frac{\partial \sqrt{\tilde{g}}\tilde{\xi}^k_\theta \bar{p}}{\partial \xi^k} + \frac{\partial \sigma^k_r}{\partial \xi^k} + \frac{1}{Re}\left[\frac{\partial}{\partial \xi^k}\left(\sqrt{\tilde{g}}\tilde{g}^{k\lambda}\frac{\partial \bar{v}_r}{\partial \xi^\lambda}\right)\right. \\ \left. -\frac{1}{r}\left(\sqrt{\tilde{g}}\bar{v}_r + 2\frac{\partial \sqrt{\tilde{g}}\tilde{\xi}^k_\theta \bar{v}_\theta}{\partial \xi^k}\right)\right]\end{aligned} \tag{5b}$$

$$\begin{aligned}\frac{\partial r\sqrt{\tilde{g}}\bar{v}_\theta}{\partial t} + \frac{\partial \overline{U}^k \bar{v}_\theta}{\partial \xi^k} - \sqrt{\tilde{g}}\bar{v}_r \bar{v}_\theta \\ = -\frac{\partial \sqrt{\tilde{g}}\tilde{\xi}^k_\theta \bar{p}}{\partial \xi^k} + \frac{\partial \sigma^k_\theta}{\partial \xi^k} + \frac{1}{\mathrm{Re}}\left[\frac{\partial}{\partial \xi^k}\left(\sqrt{\tilde{g}}\tilde{g}^{k\lambda}\frac{\partial \bar{v}_\theta}{\partial \xi^\lambda}\right)\right. \\ \left. -\frac{1}{r}\left(\sqrt{\tilde{g}}\bar{v}_\theta - 2\frac{\partial \sqrt{\tilde{g}}\tilde{\xi}^k_\theta \bar{v}_r}{\partial \xi^k}\right)\right]\end{aligned} \tag{5c}$$

where the resolvable contravariant velocity components ($\overline{U}^k$) in the convective derivatives are defined: $\overline{U}^k = \sqrt{\tilde{g}}\tilde{\xi}^k_{x_j}\bar{q}_j$. The subgrid scale (SGS) stress tensor σ^k_i is defined as $\sigma^k_i = \overline{U}^k\bar{v}_i - \overline{U^k v_i}$. According to Jordan (1999), the metric coefficients are considered as filtered because they are evaluated numerically at discrete points along the curvilinear lines (denoted by a tilde).

To resolve the duct flow, the above LES system was time-advanced by a variant of the fractional-step method (Jordan and Ragab, 1996). The technique implements a semi-staggered discretization molecule that is reformulated for boundary-fitted cylindrical coordinate domains. The diffusive derivatives were time-advanced by the Crank–Nicolson scheme to eliminate the high viscous stability restriction near no-slip walls. All the non-linear terms were time-advanced by the explicit second-order Adams–Bashforth technique. Spatially, the convective derivatives in the streamwise and radial directions were approximated by a compact fifth-order-accurate upwind-biased approximation (Jordan, 2002) while the respective circumferential terms were discretized by a fourth-order-accurate Padé stencil. All the diffusive terms were discretized using standard second-order-accurate central differences. Second-order central differencing was also used to approximate the pressure-Poisson equation of the fractional-step procedure.

3. Dynamic subgrid scale model

An eddy viscosity relationship modified for dynamic computation of the model coefficient was selected to represent the SGS stress field (Smagorinsky, 1963;

Germano et al., 1991). The dynamic improvement produces the correct asymptotic behavior of the turbulent stresses when approaching no-slip walls. Moreover, this model will also respond correctly to the low-turbulent corner regions of the troughs immediately downstream of the ribs. To implement this model for the ribbed duct simulation, each term was transformed to the computational space (Jordan, 2001). The model is expressed as

$$\sigma_i^k + 1/3\tilde{\varsigma}_i^k \tau_{\lambda\lambda} = 2C\overline{\Delta}^2 |\overline{S}|\overline{S}_i^k \tag{6}$$

where C is the dynamic coefficient and the filtered metric term $\tilde{\varsigma}_i^k$ is defined as $\tilde{\varsigma}_i^k = \sqrt{\tilde{g}}\tilde{\xi}_{x_j}^k \delta_{ij} = \tilde{\xi}_{x_i}^k$. In this model, the turbulent eddy viscosity (ν_T) is defined by $\nu_T = C\overline{\Delta}^2|\overline{S}|$ where $|\overline{S}| = \sqrt{2\overline{S}_{ij}\overline{S}_{ij}}$ and $\overline{\Delta}$ is the grid-filter width. The resolvable strain-rate field ($\overline{S}_i^k$) is expressed as $\overline{S}_i^k = \sqrt{\tilde{g}}\tilde{\xi}_{x_j}^k \overline{S}_{ij}$ with its complete definition as

$$\overline{S}_x^k = \frac{1}{2}\left(\sqrt{\tilde{g}}\tilde{g}^{k\lambda}\frac{\partial \bar{v}_x}{\partial \xi^\lambda} + f_j \tilde{\xi}_{x_j}^k \frac{\partial \sqrt{\tilde{g}}\tilde{\xi}_x^\lambda \bar{v}_j}{\partial \xi^\lambda}\right) \tag{7a}$$

$$\overline{S}_r^k = \frac{1}{2}\left(\sqrt{\tilde{g}}\tilde{g}^{k\lambda}\frac{\partial \bar{v}_r}{\partial \xi^\lambda} + f_j \tilde{\xi}_{x_j}^k \frac{\partial \sqrt{\tilde{g}}\tilde{\xi}_r^\lambda \bar{v}_j}{\partial \xi^\lambda}\right) - \frac{1}{2r}\left(\sqrt{\tilde{g}}\bar{v}_r + 2\frac{\partial \sqrt{\tilde{g}}\tilde{\xi}_\theta^k \bar{v}_\theta}{\partial \xi^k}\right) \tag{7b}$$

$$\overline{S}_\theta^k = \frac{1}{2}\left(\sqrt{\tilde{g}}\tilde{g}^{k\lambda}\frac{\partial \bar{v}_\theta}{\partial \xi^\lambda} + f_j \tilde{\xi}_{x_j}^k \frac{\partial \sqrt{\tilde{g}}\tilde{\xi}_\theta^\lambda \bar{v}_j}{\partial \xi^\lambda}\right) - \frac{1}{2r}\left(\sqrt{\tilde{g}}\bar{v}_\theta - 2\frac{\partial \sqrt{\tilde{g}}\tilde{\xi}_\theta^k \bar{v}_r}{\partial \xi^k}\right) \tag{7c}$$

where $f_j = \langle r, 1, r\rangle$. The Crank–Nicolson and Adams–Bashforth schemes were applied to the first-order and remaining components of the total viscous term, respectively, to preserve second-order accuracy in time.

4. Dynamic evaluation of the model coefficient

Deriving a unique expression for dynamic evaluation of the model coefficient starts with explicitly filtering the grid-scale LES equations (Eqs. (4) and (5)) a second time by a test filter (Jordan, 2001; Lilly, 1992). The coefficient itself is determined locally over a narrow band of finest resolved scales as given by the test filter kernel and width ($\overline{\overline{\Delta}}_t$). For computing the ribbed duct flow, a test filter that employs volume averaging (Schumann, 1975) was used with its width set at twice that of the local grid spacing: $\overline{\overline{\Delta}}_t = 2\overline{\Delta}_g$. Test filtering along the curvilinear lines can take place in either the physical domain or computational space because the coordinate transformation operation is performed prior to all required explicit filtering. When filtering in the non-uniform physical domain, one must avoid the associated second-order error by numerically evaluating each contributing first-order derivative prior to the explicit filter operation. The Leonard term (L_i^k) as originally identified by the Germano identity in Cartesian coordinates (Germano et al., 1991) has a cognate form in the computational space

$$L_i^k = T_i^k - \bar{\sigma}_i^k \tag{8}$$

where the single overbar denotes the same test filter operator. In this identity, the modified Reynolds stress (T_i^k) is defined as

$$T_i^k - \frac{1}{3}\tilde{\varsigma}_{x_j}^k T_{\lambda\lambda} = 2C\overline{\overline{\Delta}}^2 \left|\overline{\overline{S}}\right|\overline{\overline{S}}_i^k \tag{9}$$

Upon substituting the definitions for T_i^k and the test-filter SGS stress $\bar{\sigma}_i^k$ into the new identity (Eq. (8)), the eddy viscosity relationship for L_i^k becomes

$$L_i^k - \frac{1}{3}\tilde{\varsigma}_{x_j}^k L_{\lambda\lambda} = 2C\overline{\Delta}^2 M_i^k \tag{10}$$

where the model stress field (M_i^k) is defined as

$$M_i^k = \alpha^2 \left|\overline{\overline{S}}\right|\overline{\overline{S}}_i^k - \overline{|\overline{S}|\overline{S}_i^k}$$

with filter width ratio $\alpha = 2$. A convenient step intrinsic in the L_i^k model derivation is the removal of the model coefficient from the test filter operation. Although this step simplifies the derivation (and consequently facilitates the computation), implementation of the model in the computation assumes that C is spatially averaged along at least one curvilinear coordinate direction. In the present duct flow simulation, averaging of the model coefficient occurred along all the circumferential lines.

The final step for obtaining a unique expression for C involves contraction of the resolvable transformed Leonard term in Eq. (10). However, the procedure must be careful to insure rotational invariance of the coefficient in both the physical domain and transformed space. The proper procedure requires writing the error function in the physical domain before minimizing its square. The contravariant error tensor (E_i^k) along the curvilinear line in the physical domain becomes

$$E_i^k = \sqrt{\tilde{g}}\tilde{\xi}_{x_j}^k L_{ij} - \frac{1}{3}\tilde{\varsigma}_{x_j}^k L_{\lambda\lambda} - 2C\overline{\Delta}^2\sqrt{\tilde{g}}\tilde{\xi}_{x_j}^k M_{ij} \tag{11}$$

where matrices L_{ij} and M_{ij} are not summed independently. Minimizing this error gives the expression

$$C = \frac{L_i^k \cdot M_i^k}{2\overline{\Delta}^2 M_m^k \cdot M_m^k} \tag{12}$$

for the model coefficient, which operates on the inner product of the Cartesian tensor components of L_i^k and M_i^k in the computational space.

Inasmuch as the model coefficient is dependent on the local instantaneous strain-rates of the resolved field, either positive or negative values are possible in its evaluation. While the positive coefficients denote forward scatter in the turbulent energy spectrum, the negative

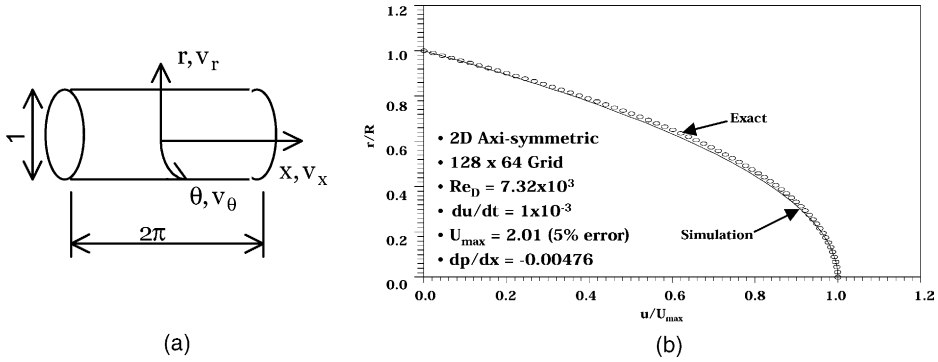

Fig. 2. Test simulation of laminar pipe flow: (a) canonical pipe flow geometry; (b) streamwise velocity profile.

values symbolize backscatter, or the reverse of energy from the SGS scales to the finest scales of the resolved field. Experience has demonstrated that the backscatter physics correlate well over long execution times, which quickly demand "ad hoc" measures to guarantee stability. However, in most simulations the statistical contribution of the SGS model is usually small compared to the resolved fields. Thus, the best choice for maintaining a stable computation at the instantaneous level is to truncate all negative contributions from the dynamic model to yield a net zero effect.

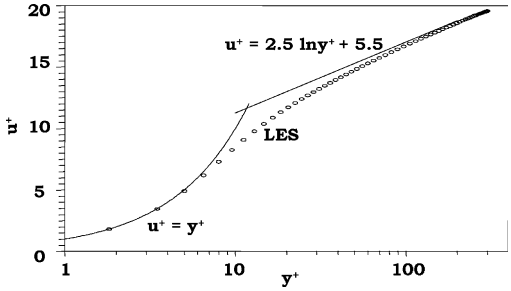

Fig. 3. Test simulation of turbulent pipe flow.

5. Simulation results and discussion

The following section presents and discusses the turbulent statistics of a roughened cylindrical duct by square symmetric ribs placed periodically at intervals $p/h = 5$. These statistics were computed using the LES methodology for a duct flow with $Re_D = 8000$ (or $Re_\theta = 720$). Contrary to most choices for p/h where the focus is on optimizing turbulent mixing, the present computation is first concerned with the rib's detrimental effect on the static pressure. Specifically, the interval $p/h = 5$ is chosen according to the experimental evidence (Berger and Hau, 1979) for minimizing the pressure recovered in a rib duct. Comparisons of the LES results to full-scale data are presented in the latter paragraphs of this section. The measurements depict 'at-sea' testing of the static pressure and mean velocities as collected inside a roughened vehicle launchway on-board a US Navy submarine. Although the respective Reynolds numbers within the vehicle launchway are several orders higher than the present simulation, the similarity of physics will indicate equivalent non-dimensional quantities of practical importance.

Before presenting the LES results of the ribbed-wall duct, velocity profiles of two initial simulations are plotted in Fig. 2 (laminar flow) and Fig. 3 (turbulent flow) involving the canonical pipe flow. The impetus of these computations was verification of the formulation accuracy and its numerical stability in view of the high-order compact stencils used to approximate the convective derivatives. Both the streamwise (axial) and circumferential boundary conditions are periodic in these simulations. Given a fixed streamwise pressure gradient of $dp/dz = -0.00476$, the laminar flow computation gave a 5% error of the centerline velocity for a coarse stretched grid. The turbulent flow computation followed the published results of Eggles et al. (1994) as listed in Table 2 in wall units, but with 1/2 the number of grid points in the streamwise and circumferential directions. One can see that the present simulation correctly predicted the inner and overlap layers of this flow.

Table 2
Table of parameters for test and referenced simulations of turbulent pipe flow

Grid	u_τ	Re_τ	Re_c	y^+	η^+
$256\times96\times128$[a]	0.017	360	6950	0.94	1.6
$128\times128\times64$	0.018	381	7400	1.01	1.5

[a] Ref. Eggles et al. (1994).

5.1. Grid resolution for ribbed-wall circular duct

The space limitations of the submarine launchway dictated the maximum permissible height to diameter ratio (h/D) of each rib. Accordingly, both the simulation and 'at-sea' measurements reflect turbulent ingestion into the core flow for symmetric ribs with $h/D = 0.115$

and $s/D = 0.575$. Proper resolution of the turbulent character near each rib requires respective boundary stretching of the grid lines. Choice of the first field point is difficult to justify 'a priori' because the classic law-of-the-wall profile is not expected along any of the duct walls (expect perhaps near the rib crests). Typically, the first field point in wall units should be on the order of $y^+ < 5$. Using this criterion as a requirement on the instantaneous level, the grid cluster was suitably adjusted before collection of the LES results took place for evaluating the steady-state turbulent statistics.

The final grid reached for the cylindrical rib application housed $65 \times 141 \times 401$ points in the circumferential (θ), radial (r), and streamwise directions (z), respectively, as shown in Fig. 4 with simulation parameters listed in Table 3. The grid was orthogonal, but boundary-fitted to all no-slip walls. First point spacing around the ribs was 0.013 (scaled by h). Along the cylinder walls in the trough region the first point spacing was 0.021. Highest mean values for y^+ were found along the rib crests and typically were $y^+ = \mathrm{O}(1)$.

Although the instantaneous flow is obviously non-periodic, the computation assumed statistical steady-state homogeneous characteristics at each subsequent rib and trough section. To judge the time required to steady-state, two ribs were simulated with periodic boundary conditions in the streamwise as well as the circumferential directions. The grid spacing in the circumferential direction was uniform over $0 \leqslant \theta \leqslant 2\pi$. Statistical steady-state was reached at $T = 32$ ($\Delta T = 0.001$), where $T = tU_c/h$ which is based on the mean centerline streamwise velocity (U_c). At statistical steady-state, $Re_D = 8000$ with $Re_\theta = 720$ using either the radial profiles over the crests or trough regions.

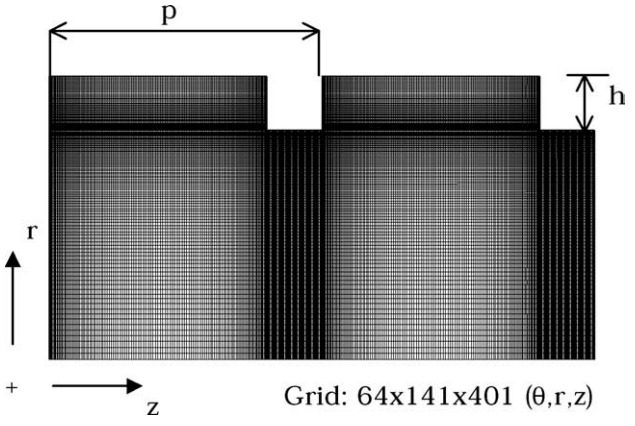

Fig. 4. Profile of the structured grid used for the LES computation of the ribbed-wall circular duct.

Table 3
Geometric and flow conditions for the LES computation of the ribbed-wall duct

h/D	p	Δy_{min}	y^+	Re_θ
0.115	5 h	0.013 h	0.75	720

5.2. Structural content inside the ribbed-wall circular duct

A snapshot of the streamwise flow structure within the ribbed-wall circular duct is illustrated in Fig. 5 in the form of isosurfaces of the vorticity magnitude ($\Omega = \sqrt{\omega_\theta^2 + \omega_r^2 + \omega_z^2}$) and contours of the circumferential vorticity (ω_θ) plotted on a typical z–r plane. While positive magnitudes are plotted in the lower half of the duct (a), negative isosurfaces are shown in the upper half (b). Away from the walls near the duct core, both figures clearly indicate elongated self-similar structures that are periodic and appear to originate near the rib crests. In the trough regions the same periodicity is apparent, but the structural shape and location of the specific vortices differ in each region. These same characteristics can be seen where the streamwise contours of ω_θ are plotted on plane $\theta = \pi/2$. The figure clearly indicates that the streamwise vortical structures do indeed originate at the rib crests and require about two periodic lengths before fully convected radially to the primary duct core. These structures house the maximum and minimum magnitudes of circumferential vorticity in the entire duct flow. Between these salient streamwise structures, a secondary low-vorticity flow exits, but the origin of these secondary structures is not readily obvious. Lastly, the distribution of circumferential vorticity in both trough regions reveals little similarity and contributes modestly to the primary vortical flow.

Snapshots of the streamwise vorticity (ω_z) above the first rib mid-plane (a) and on a second plane that is 1/2 h downstream of the first rib (b) are shown in Fig. 6. Positive streamwise vorticity is indicated by the solid contours whereas the negative values are plotted as dashed lines. Above the rib mid-plane, a circumferential cluster of streamwise structures is clearly evident that was radially convected approximately one rib height since their origin along the previous rib crest. A second cluster can be observed near the primary core flow. Unlike their lower counterpart, these latter structures only fluctuate about their mean position while being convected downstream by the streamwise core flow. The plane downstream of the first rib shows the same lower cluster of streamwise structures as seen in the previous plane. Moreover, this plane reveals the circumferential cluster of streamwise vorticity that was produced just upstream along the rib crest. Careful look at their circumferential distribution shows pairs of vortical structures of alternating sign. This observation suggests that these structures are pairs of counter-rotating streamwise vorticity. Extremely low levels of streamwise vorticity are indicated in the trough region (inside the thick

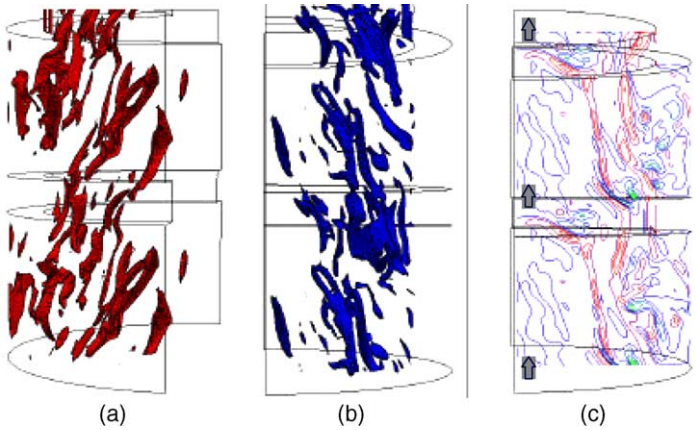

Fig. 5. Lower and upper half isosurfaces and contours of vorticity: (a) lower half isosurfaces—max. 2.4, min. 1.6, incr. 0.2; (b) upper half isosurfaces—max. −1.2, min. −2.0, incr. 0.2; (c) contours—max. 5.0, min. −6.0, incr. 1.0.

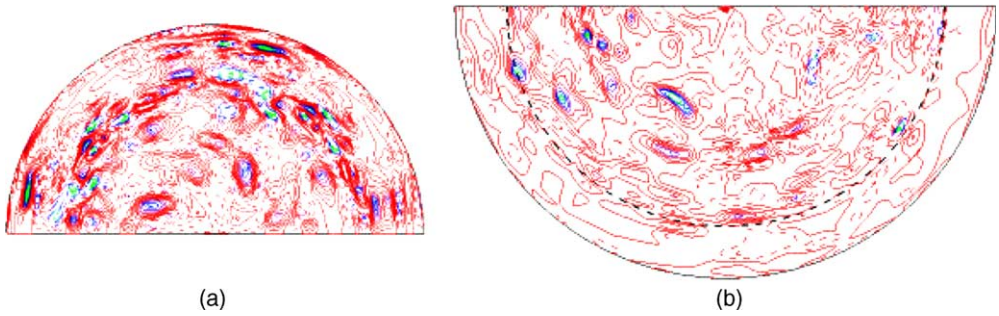

Fig. 6. Contours of instantaneous streamwise vorticity on r–θ planes above the first rib and inside the trough regions: (a) first-rib mid-plane—contours: max. 3.2, min. −2.4, incr. 0.2; (b) distance $h/2$ downstream of first rib—contours: max. 4.0, min. −4.0, incr. 0.4.

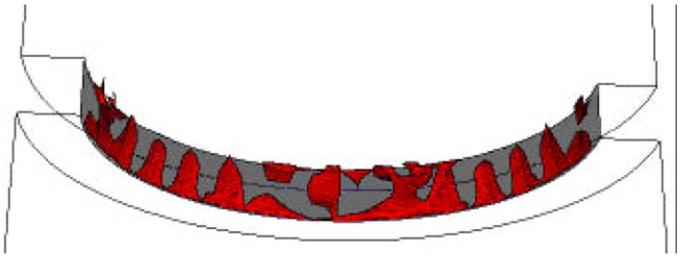

Fig. 7. Isosurfaces of instantaneous vorticity magnitude ($\Omega = 2$) above the first rib crests.

dashed lines). Specifically, the contours average about an order of magnitude less than the adjacent flow that lies above the rib crests. This observation rests on the fact that the radial component of the convective velocity lifts the streamwise vorticity from the rib crests toward the duct core, which inhibits discernable interaction in the trough regions.

We can easily explore the claim of generated counter-rotating vortical pairs above the rib crests by examining the respective circumferential distribution of vorticity magnitude. In Fig. 7, six pairs of vortical structures are clearly evident that appear symmetric about the crest streamwise centerline. Moreover, the chief content of vorticity in these structures originates immediately at the rib's leading edge.

5.3. Steady-state turbulence statistics

Fig. 8 shows the turbulence steady-state statistics scaled by the mean bulk velocity (U_b). These contours depict circumferential averages as well as time averages over $T = 32$. Also, they constitute the sum of the resolved as well as the SGS fields where the latter elements typically account for less than 10% of the total statistic. The periodicity of each quantity in the trough and core sections of the duct justifies implementing periodic boundary

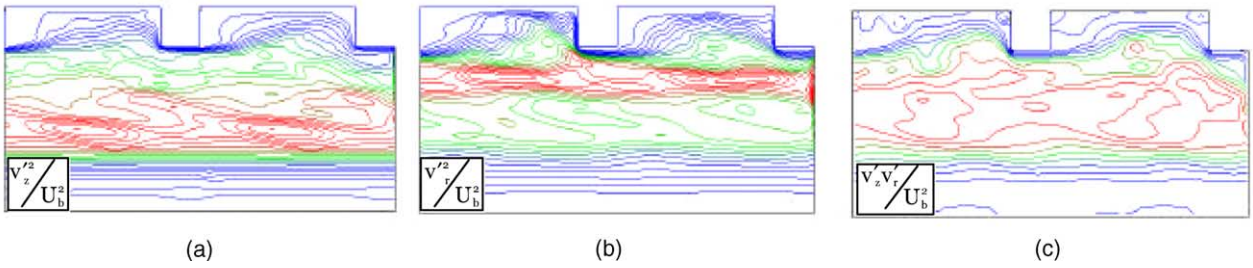

Fig. 8. Contours of statistical steady-state turbulent intensities—(a) streamwise intensity; max. 0.16, min. 0, incr. 0.008; (b) radial intensity; max. 0.06, min. 0, incr. 0.003; (c) Reynolds stress; max. 0.04, min. 0, incr. 0.0025.

conditions in the streamwise direction as well as the total time required to reach statistical steady-state. Interestingly, these intensities reach their highest levels along different narrow bands, but still within the core flow. Highest streamwise fluctuations $(v_z'/U_b)^2$ peaked at approximately $2h$ above the rib crests whereas the respective radial component $(v_r'/U_b)^2$ attains its maximum at about $\frac{1}{2}h$ into the core flow. In view of all three intensities (including the circumferential component), the streamwise fluctuations account for approximately 60% of the highest turbulent kinetic energy detected within the core flow.

Contrary to the turbulence intensities, the statistical averages of the Reynolds stress component $(v_z'v_r'/U_b^2)$ indicate a much wider band of concentrated stress within the duct core flow, with the range of values on the same order as the radial intensity. The contours also suggest growth of the rib's separated shear layer into the trough regions, which abruptly terminates due to the presence of the next rib. At the leading edge of the rib, this particular Reynolds stress attains its peak levels. Finally, minimal turbulent activity is shown in the trough and centerline regions of the duct, which were not unexpected characteristics for this type of flow.

Cursory examination of the statistical steady-state turbulence production $\langle P\rangle$ inside the ribbed duct in Fig. 9a reveals the same periodicity detected for the turbulence intensities. Although small pockets of concentrated turbulence production is discernible in the core flow, their levels are essentially on the same order of magnitude as the adjacent core regions. Most of the turbulence produced for the ribbed duct flow is actually concentrated in close proximity to the crest leading edge as illustrated in Fig. 9b. These contours denote production levels that are two orders of magnitude above that produced in the duct core. Spatial distribution of each contributing term in the production equation next to the first rib is shown in Fig. 10 with their averaged numerical values throughout the duct listed in Table 4. The dashed contours in the figures indicate negative contributions. Local comparisons among each term disclose clear differences in their spatial extent, but when scaled by the duct core area their significant levels are strictly attributed to the sharp leading edge of the rib crest.

The maxima, minima, and core averages (in percent) listed in Table 4 are scaled by the averaged turbulence production as taken throughout the entire duct flow (Fig. 9a). Outside of the circumferential component, each term indicates peak negative levels that exceed the positive contributions in magnitude. This result is largely attributed to the mean strain rates computed on the z–r surfaces adjacent to the leading edge. The columns of maxima and minima denote that the turbulence produced by the product of the radial turbulent intensity and the respective strain rate $(\langle v_r'v_r'\rangle\langle S_{rr}\rangle)$ lead all other components. However, its average is the lowest of all components, which suggests that significant contribu-

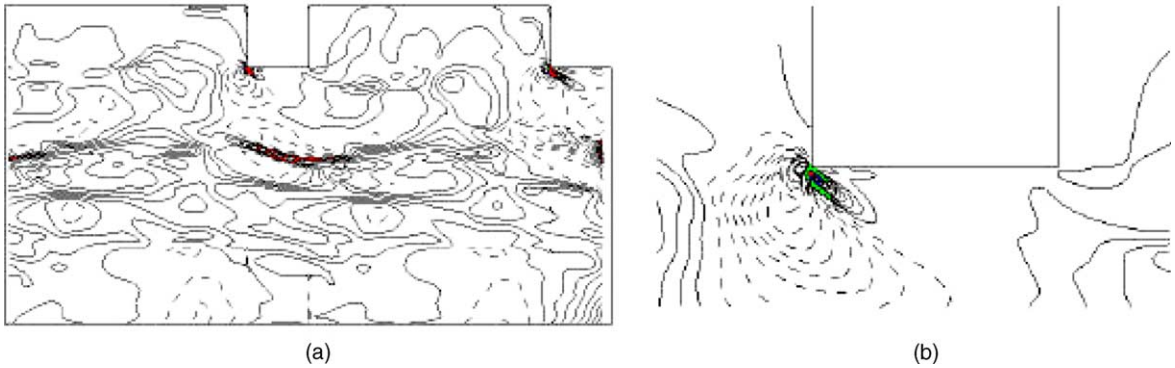

Fig. 9. Averaged turbulence production $\langle P\rangle$ computed for the ribbed duct, $\langle P\rangle = -\langle v_i'v_j'\rangle\langle \bar{s}_{ij}\rangle$: (a) duct $\langle P\rangle_{avg} = 7.24\times10^{-4}$; (b) near rib $\langle P\rangle_{peak} = 5.72\times10^{-2}$.

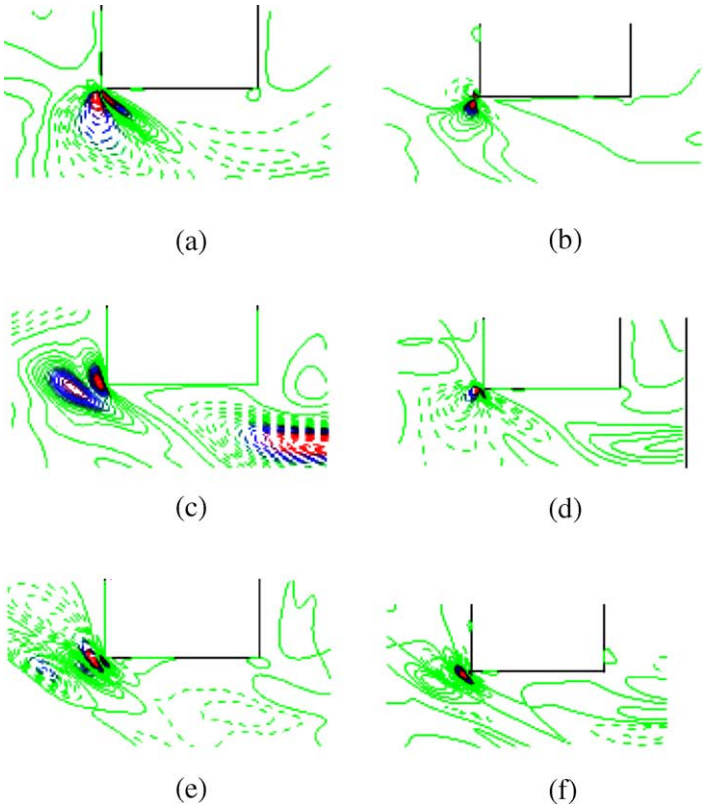

Fig. 10. Contours of each term of the turbulent production equation; scaled maxima and minima for each term are listed in Table 4: (a) $\langle u'_z u'_z \rangle \langle S_{zz} \rangle$, (b) $\langle u'_r u'_r \rangle \langle S_{rr} \rangle$, (c) $\langle u'_\theta u'_\theta \rangle \langle S_{\theta\theta} \rangle$, (d) $\langle u'_z u'_r \rangle \langle S_{zr} \rangle$, (e) $\langle u'_z u'_\theta \rangle \langle S_{z\theta} \rangle$, (f) $\langle u'_r u'_\theta \rangle \langle S_{r\theta} \rangle$.

Table 4
Maxima, mimima and averaged (scaled by $\langle P \rangle_{avg}$) values of each term in turbulent production equation

Term	Max.	Min.	AVG. (%)
$\langle P \rangle$	67	−112	100
$\langle v'_z v'_z \rangle \langle S_{zz} \rangle$	28	−68	−23.3
$\langle v'_r v'_r \rangle \langle S_{rr} \rangle$	45	−128	1.1
$\langle v'_\theta v'_\theta \rangle \langle S_{\theta\theta} \rangle$	3	−0.3	1.6
$\langle v'_z v'_r \rangle \langle S_{zr} \rangle$	30	−85	111
$\langle v'_z v'_\theta \rangle \langle S_{z\theta} \rangle$	14	−8	8.3
$\langle v'_r v'_\theta \rangle \langle S_{r\theta} \rangle$	6	−12	1.3

tions of this term to the produced turbulence in the duct is restricted to regions only near the rib leading edge. From the global average perspective, the shear component ($\langle v'_z v'_r \rangle \langle S_{zr} \rangle$) on the z–r plane is the dominant factor.

5.4. '*At-sea*' *measurements*

As noted earlier, a prototype assembly that consisted of a periodic series of seven circumferential ribs and four longitudinal lands was installed on board a US submarine for the purpose of controlling the pressure gradient inside the vehicle launchway. The submarine launchway provided a suitable means to test the effectiveness of the device because this circular duct holds a substantial flow rate once its forward end is exposed to the external hull seawater. The flow stagnates at the aft end of the duct before it is redirected to the launchway recess volume. The prototype itself was designed solely from the LES results of which the design sketch and 'as-built' assembly is shown in Fig. 11. Differential pressure sensors were mounted after the rib assembly directly in line where the flow stagnates. A flow meter for collecting the duct velocity at four radial points was placed after the fourth rib. Further information regarding the specific 'at-sea' data and their respective measurements systems can be found in the report by Jordan et al. (1999).

A welcomed improvement of the prototype device was the correction of the flow irregularity that was originally detected in the streamwise velocity profiles. As shown in Fig. 12, the scaled profiles displayed different degrees of asymmetry that depended strongly on the submarine speed with the forward end of the duct exposed to the external flow field. Inasmuch as the consistency of the recovered pressure (or friction coefficient) is a quadratic function of the bulk velocity Eq. (1), the violation of scale-similarity of the velocity profiles leads to a large measurement error in the respective coefficients. Conversely, the circumferential ribs regulate the flow such that non-dimensional velocity profiles exist over a wide range of flow rates. The profiles follow a power-law distribution that is easily integrated to compute the bulk velocity through the duct. Given a

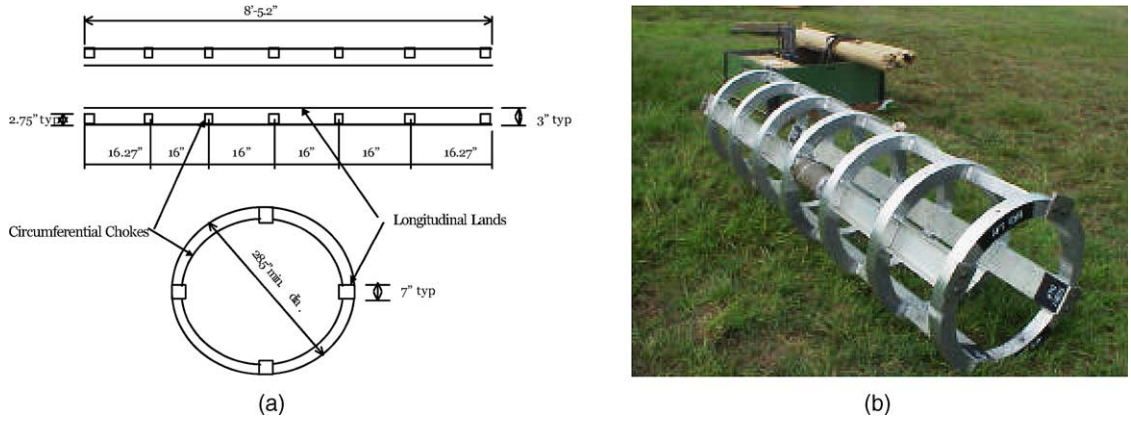

Fig. 11. Sketch and 'as-built' prototype assembly for velocity and pressure measurements on board a US Navy submarine: (a) prototype sketch; (b) 'as-built' prototype.

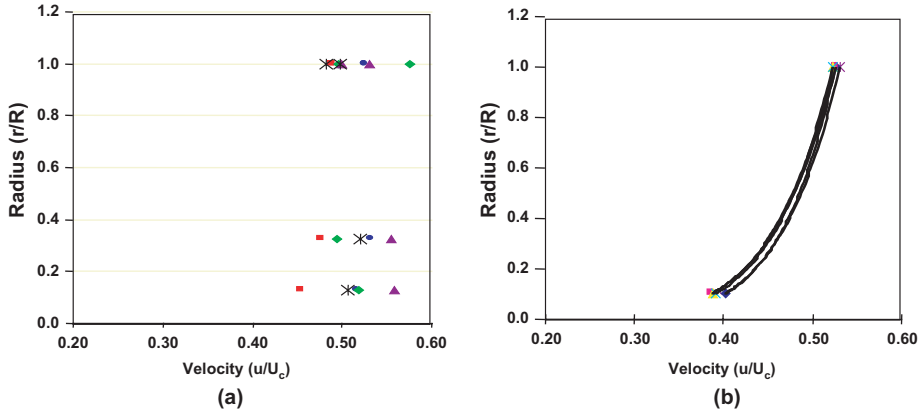

Fig. 12. Comparison of streamwise velocity profiles without and with circumferential ribs inside the launchway duct; symbols of different shape denote different submarine speeds: (a) duct without rib assembly; (b) duct with rib assembly.

consistence set of velocity profiles, the recovery coefficients are not only scale-similar but also more reliable.

The argument posed for placing periodic ribs in the launchway duct was to control the pressure recovered by turbulent ingestion. This quantity was calculated for the launchway flow by using the measured pressure differences with and without the periodic rib prototype assembly installed in the duct. Although pressure measurements were taken over five submarine speeds, only three gave useful data. Fig. 13a is a plot of the calculated

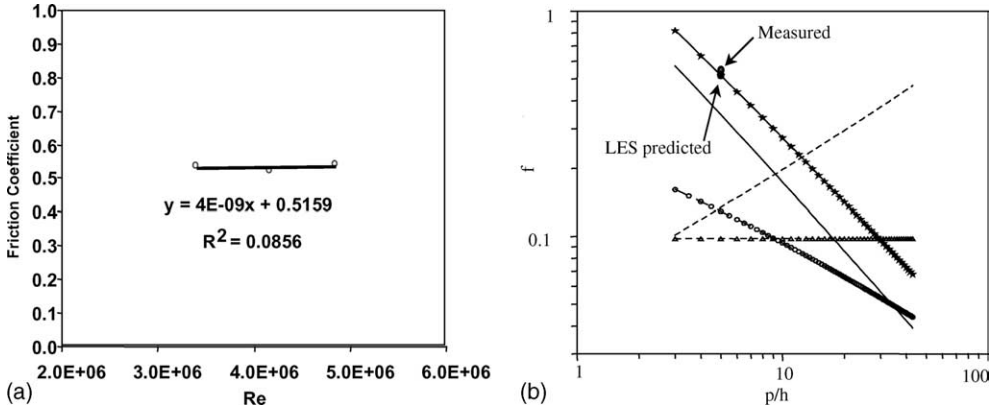

Fig. 13. Friction coefficients (based on core pressure gradient) determined from the measured pressure reductions inside the launchway duct and LES results: (a) friction coefficient in launchway duct—three data points denote separate submarine speeds; (b) comparison of measured and predicted friction coefficients.

friction coefficients over Reynolds numbers $3.2 \times 10^6 \leqslant Re_D \leqslant 4.6 \times 10^6$ according to the relationship $f = 2\Delta p/\rho u_b^2 (D/L)$, where L is the streamwise length of the prototype. Given the similarity of the velocity profiles, the corresponding range of Reynolds numbers based on the momentum thickness (θ) as the length scale is $1.9 \times 10^4 \leqslant Re_\theta \leqslant 2.8 \times 10^4$. A linear least-squares fit to the data points in Fig. 13a shows an intercept of $f = 0.52$ with a negligible slope and a 0.09 R-squared value. Using the mean pressure gradient from the LES results at the duct centerline, a friction coefficient of $f = 0.51$ was calculated which is shown in Fig. 13b along with launchway flow value. After comparing these coefficients we can conclude that although the at-sea measurements were taken at Reynolds numbers three orders of magnitude higher than the present LES results, their agreement illustrates the fact that the salient turbulent physics responsible for the pressure loss are consistent in each case.

6. Final remarks

A cylindrical duct roughened by 'k-type' periodic square ribs at $p/h = 5$ was simulated by the LES methodology and subsequently 'at-sea' tested inside the vehicle launchway on board a US Navy submarine. The structural content of this duct flow shows pairs of counter-rotating vortices formed at the leading edge of the rib crest that are quickly convected toward the duct core. Soon after the next rib, these elongated structures have reached their final streamwise destination within the core flow. The troughs that lie between subsequent ribs are essentially benign turbulent regions in view of the adjacent core. However, contours of significant shear stress $\langle v_z' v_r' \rangle$ confirm the observations by Berger and Hau (1979) where the downstream separated shear layer nearly reattaches before deflected by the next rib.

The turbulence ingested by the core flow that accounts for an irrecoverable pressure loss in the duct is produced largely at the rib crest leading edge. In particular, the peak turbulence levels in this vicinity are two orders of magnitude higher than the duct global average. Locally near the leading edge, the radial turbulent production term $\langle v_r' v_r' \rangle \langle S_{rr} \rangle$ is the dominant source. But from the global perspective, the shearing term $\langle v_z' v_r' \rangle \langle S_{zr} \rangle$ clearly shadows all other terms in the turbulence production equation.

The Reynolds numbers of the LES simulation and 'at-sea' measurements differ by nearly three orders of magnitude ($Re_D^{sim} = 8 \times 10^3$ versus $(Re_D^{exp})_{avg} = 4 \times 10^6$, respectively). Despite this large disparity, their core pressure loss in terms of a frictional coefficient at the duct centerline was essentially equivalent for both duct flows. The agreement suggests that the salient turbulent physics produced at both Reynolds numbers are essentially the scale-similar. Notably, the previous asymmetric character of the launchway flow became well organized and self-similar after passing over the second rib. This improvement facilitated evaluation of a unique bulk velocity value for determining the frictional coefficient of the full-scale prototype.

Acknowledgements

The author wishes to thank L.P. Purtell (program officer, Office of Naval Research, Code 333), Contract number N0001401WX20981 and R.B. Philips (NUWC, Code 10) for their support of LES research related to flow over roughened surfaces. The data that was collected on board the USN submarines was supported by the Naval Sea Systems Command (CDR. F.F. Schulz, PMS-350). Finally, this work was supported in part by a grant of HPCMP resources from the Arctic Region Supercomputing Center.

References

Berger, F.P., Hau, K.F., 1979. Local mass/heat transfer distribution on surfaces roughened with small square ribs. Journal of Heat Mass Transfer 22, 1645–1656.

Eggles, J.G.M., Unger, F., Weiss, M.H., Westerweel, J., Adrian, R.J., Friedrich, R., Nieuwstadt, F.T.M., 1994. Fully developed turbulent pipe flow: a comparison between direct numerical simulation and experiment. Journal of Fluid Mechanics 268, 175–209.

Germano, M., Piomelli, U., Moin, P., Cabot, W.H., 1991. A dynamic subgrid-scale eddy viscosity model. Physics of Fluids A 3, 1760–1765.

Han, J.C., 1988. Heat transfer and friction characteristics in rectangular channel with rib tabulators. Journal of Heat Transfer 110, 321–328.

Jordan, S.A., 1999. A large-eddy simulation methodology in generalized curvilinear coordinates. Journal of Computational Physics 148, 322–340.

Jordan, S.A., 2001. Dynamic subgrid-scale modeling for large-eddy simulations in complex topologies. Journal of Fluids Engineering 123, 1–10.

Jordan, S.A., 2002. Resolving turbulent wakes. Paper FEDSM2002-31282, ASME 2002 Fluids Engineering Summer Meeting, Montreal, Quebec, Canada.

Jordan, S.A., Ragab, S.A., 1996. An efficient fractional-step technique for unsteady three-dimensional flows. Journal of Computational Physics 127 (0170), 218–225.

Jordan, S.A., Gieseke, T.J., Guillmette, N.H., Ryan, P.J., Griffen, R.J., 1999. Reverse flow in the Torpedo launch system of the seawolf-class submarine. NUWC-NPT Technical Report 11,102, Naval Undersea Warfare Center, Newport, RI.

von Karman, T., 1930. Nach. Ges. Wiss. Goett. Math.-Phys. Kl., 58–76.

Keirsbulck, L., Labraga, L., Mazouz, A., Tournier, C., 2002. Surface roughness effects on turbulent boundary layer structures. Journal of Fluids Engineering 124, 127–135.

Lilly, D.K., 1992. A proposed modification of the germano subgrid-scale closure method. Physics of Fluids A 4, 633–635.

Okamoto, S., Seo, S., Nakaso, K., Kawai, I., 1993. Turbulent shear flow and heat transfer over the repeated two-dimensional square ribs on ground plate. Journal of Fluids Engineering 115, 631–637.

Perry, A.E., Schofield, W.H., Joubert, P.N., 1969. Rough wall turbulent boundary layers. Journal of Fluid Mechanics 37, 383–413.

Schumann, U., 1975. Subgrid-scale model for finite difference simulation of turbulent flows in plane channel and annuli. Journal of Computational Physics 18, 376–404.

Smagorinsky, J., 1963. General circulation experiments with the primitive equations, I. The basic experiment. Monthly Weather Review 91, 99–164.

Wassel, A.T., Mills, A.F., 1979. Calculation of variable property turbulent friction and heat transfer in rough pipes. Journal of Heat Transfer 101, 467–474.

Webb, R.L., Eckert, E.R.G., Goldstein, R.J., 1971. Heat transfer and friction in tubes with repeated ribs roughness. Journal of Heat and Mass Transfer 14, 601–618.

Whitehead, A.W., 1976. The effects of surface roughening on fluid flow and heat transfer. PhD Thesis, Queen Mary College, University of London.